Journal of Scientific & Industrial Research
Vol. 84, June 2025, pp. 688-702
DOI: 10.56042/jsir.v84i6.8731

Designing and Spectral Investigations of S-benzyl β-(N-3-(2-nitrophenyl)allylidene)dithiocarbazate as a potential 2019-nCoV main Protease Inhibitor

Rayees A Bhat[1]*, Kaman Singh[2], Gajanan Pandey[2], D Kumar[3], Ashok S Chouhan[3], Prashant Mishra[4], Utkarsh Dixit[2], Mehraj U Bhat[5], Presenjit[2] & Vimalesh Kumar Singh[6]

[1]Department of Chemistry, GLA University, Mathura 281 406, Uttar Pradesh, India

[2]Department of Chemistry, Babasaheb Bhimrao Ambedkar University, Lucknow 226 025, Uttar Pradesh, India

[3]Centre of Research for Chemical Sciences, Govt Model Science College, Jiwaji University, Gwalior 474 009, Madhya Pradesh, India

[4]Department of Chemistry, National Post Graduate College (An autonomous college), Lucknow 22 6001, Uttar Pradesh, India

[5]Department of Chemistry, Marri Laxman Reddy Institute of Technology and Management, Dundigal, Hyderabad 500 043, Telangana, India

[6]Department of Chemistry, Dr. Ambedkar Government College Unchahar Raebareli Uttar Pradesh 229 404, India

Received 12 February 2024; revised 12 September 2024; accepted 19 May 2025

The current work reports NS Schiff base S-benzyl β-(N-3-(2-nitrophenyl)allylidene)dithiocarbazate (HL) formulated as $C_{17}N_3O_2S_2H_{15}$. The synthesized Schiff base ligand (HL) was investigated by ^{1}HNMR, FT-IR, mass, Raman and UV-Vis analysis. The binding energies (−ΔG) of HL for DNA, proteins (3C5W) & main protease (7BRO) were −19.6648, −20.5016 & −4.8 kj/mol., docking study showed significant therapeutic proficiency of (HL) to be used as 2019-nCoV main protease inhibitor. Anti-bacterial activity of (HL) has been checked against two multi-resistant bacterial strains *E. coli* (Gram −ve) and *S. aureus* (Gram +ve) showing notable bacteriostatic activity. The thermal stability of (HL) was studied by heating the (HL) at controlled rate of 15ºC per minute under N_2 atmosphere, up to the temperature range of 500°C. To support experimental findings theoretical investigation of (HL) was performed with the DFT-RB3LYP calculation method using basis set 6−311++G (D,P) for geometry optimization found −1536.98 a.u minimum energy and dipole moment 5.8005 Debye. FT-IR, Raman, and UV-Vis were perlustrated by both experimental and theoretical techniques. VEDA−4 software package was involved to scrutinize the percentage contribution of different segments from (HL) in FT-IR spectra obtained by Gaussian09 software. Comprehensive observations identified 111 fundamental vibrational modes, along with the potential energy distribution percentage (PED%) for each vibration and from dihedral angle calculations, indicating that HL possesses a non-linear geometry. This research explores novel bioactive alkyl/aryl NS chelating metal complexes as single crystals to enhance nano-bio interactions and expand electronic applications.

Keywords: 2019-nCoV, Antibacterial, DFT, Docking, Protease-inhibitor

Introduction

Microbial infection is triggering stern complications on animal and human beings in the world during past few decades. Number of modifications has been carried out by medicinal chemists by connecting various active compounds with dithiocarbazate moiety creating access to various biological activities. NS-based Schiff base precursors are an intriguing group of organic compounds and the compounds formed from dithiocarbazates having (C = N) group is of immense interest because of its stability, chelating properties and biological applications. Curtis was the first to report the synthesis of dithiocarbazic acid.[1] Since then, a large number of Schiff bases of dithiocarbazic acid bearing S-alkyl/aryl-esters have been synthesized by various workers.[2,3] Due to Sustainable biological and medicinal importance of dithiocarbazate Schiff base ligands, they have received conventional significance. Because of varying magnetic character, spectroscopic properties and unusual stereochemistry of nitrogen-oxygen comprising Organic frameworks has been studied extremely with diverse transition metals. Among sulphur and nitrogen of dithiocarbazate Schiff base ligands, existence of sulphur as donor atom have been explored widely because of its noteworthy biological efficacy as vizanti tumor antifungal insecticidal antibacterial compounds, non-linear optical (NLO) materials[4], solar cell machineries and nano-materials.

*Author for Correspondence
E-mail: rayeesbinahad@gmail.com

Due to their chemical stability and biological activity, dithiocarbazates are known to elicit a wide range of biological responses. This has prompted synthetic chemists to prepare and pharmacologically evaluate numerous dithiocarbazate Schiff-base ligands and metal complexes. Some of these have emerged as important core structural subunits in drug molecules. These sulphur and Nitrogen bearing ligands form bidentate-chelates with both main group and transition metals via soft S and hard N donor sites. Schiff bases form promising derivatives with aldehydes, for instance of Trans-o-Nitrocinnamaldehyde or vanillin (4-hydroxy-3-methoxybanzaldehyde) can introduce supplementary oxygen donor site, then matching tridentate ligands works very well, with the Nitro-benzene or methoxy-benzene ring which enhances the biological activity potential of required Schiff base ligands. In the field of mineral processing, removal of heavy metal ions from aqueous solutions, and contaminated water by a simple ionic flotation method or simply by adsorption method, the dithiocarbazate and its derivatives show profound applications. These ligands on mineral surfaces potentially form metal complexes and make the mineral surfaces more hydrophilic and the flotation of specific minerals decreases in the flotation separation process. The chemistry of nitrogen-sulfur chelating ligands was first reviewed by Ali and Livingstone in the 1970s. Since then, these compounds have garnered significant interest from researchers due to their structural diversity and ion-sensing capabilities. Consequently, organic metal complexes of Schiff bases have involved countless attention.[4] Transition metal complexes of S-allyl, S-methyl, S-benzyl dithiocarbazate Schiff base containing 4-hydroxy-3-methoxybanzaldehyde, 2, 4, 5-trimethoxy benzaldehyde, 4-fluoro-banzaldehyde studied for their antimicrobic action against some pathogenic bacteria (*S.-β-haemolyticus*, *K. pneumoni*, and *E. coli*) and fungi (*A. fumigates*, *A. niger* and *C. albicans*).[5,6] Protein-ligand interactions are extensively investigated for the development of drug delivery agents, as protein-bound pharmaceuticals are expected to represent the next generation of therapeutics. Proteins transport and safeguard highly unstable cytotoxic chromophores that react with DNA, leading to strand breakage. Conversely, protein-drug interactions can diminish drug efficacy. The specificity of binding and the capacity to release a drug are influenced by the precise encapsulation of drugs within the three-dimensional pockets of protein structures. The interaction of geometric isomers with proteins is particularly captivating, as examining these associations can enhance understanding of the role of proteins in drug delivery. Although various nitrogen-sulfur (NS) chelating compounds have been assessed across multiple biological fields, only a limited number of studies have focused on pure ligands and their theoretical efficacy in inhibiting the main protease.

In continuation of research work, in this article, research-group reported the designing, characterization, molecular docking especially for 2019-nCoV main protease inhibitor, biological activity, Thermal stability, and In-silico properties of S-benzyl β-(N-3-(2-nitrophenyl)allylidene)dithiocarbazate (HL). Scheme 1, is the result of condensation reaction between trans-o-nitro cinnamaldehyde and S-benzyl dithiocarbazate.

Experimental

Materials and Methods

Hydrazine hydrate and carbon disulfide were sourced from LOBA Chemie; benzyl chloride and potassium hydroxide from Qualigens; and trans-O-nitrocinnamaldehyde from Sigma Aldrich. All solvents used were reagent grade, distilled, and dried under a nitrogen atmosphere prior to use. Reaction progress was monitored by thin-layer chromatography (TLC) using commercial silica gel (60–120 mesh) and spots were visualized under UV light.

FTIR spectra were recorded on a PerkinElmer FTIR-105627 (4000–400 cm^{-1}) in KBr discs. ^{1}H-NMR and ^{13}C-NMR were performed using a JEOL-400YH spectrometer. Mass spectrometry was conducted with a Q-TOF LC/MS, and Raman spectra were obtained with a JYH LABRAM-HR (400–1100 nm). Electronic spectra of S-benzyl β-(N-3-(2-nitrophenyl) allylidene) dithiocarbazate (HL) having conc. 10^{-3}M in acetone were captured using T60 UV–

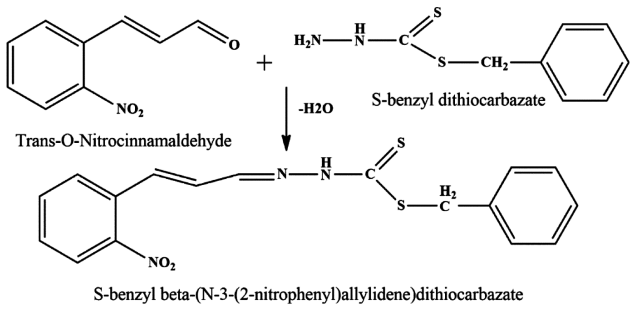

Scheme 1 — Synthesis of S-benzyl β-(N-3-(2-nitrophenyl) allylidene)dithiocarbazate

Vis spectrophotometer (200–800 nm). Thermal analysis was done using a TGA-50 SHIMADZU-00652 under N_2 atmosphere, heating rate 10°C/min. NMR samples in $CDCl_3$ solvent.

Synthesis of S-Benzyl β-(N-3-(2-nitrophenyl)allylidene) dithiocarbazate (HL)

A fresh solution of S-benzyldithiocarbazate[7] (1.98 g, 0.01mmol) was mixed with a boiling solution of trans-o-nitrocinnamaldehyde (1.78 g, 0.01 mmol) in 17 mL of boiling ethanol. The mixture was refluxed for 1 hour on a water bath, yielding a reasonable amount of product, as adapted from previously reported literature. Microcrystals of the light orange compound were subsequently isolated.[8,9] Despite extensive efforts, single crystals of the desired dithiocarbazate Schiff base have yet to be obtained.[10,11]

Computational Methodology

Density functional theory-based geometrical optimization were performed by RB3LYP method & [6-311++G(D,P)] basis set level without any symmetry constraints at −1536.98 a.u total energy. Zero imaginary frequency suggests that the compound is at its local minima. The optimized configuration was further employed for IR, UV-Vis, and NMR analysis. Computational UV-Vis absorption scanning of (HL) calculated by TD-DFT method and employed basis set RB3LYP 6-311++G(D,P). The Gaussian09 (G09) quantum chemical software was used for all the theoretical calculations.[12] VEDA-4 (Vibrational energy distribution analysis) package and GaussSum package were used for detailed analysis of IR and UV-Vis results obtained from G09 package.

Vibrational Analysis

The geometry optimizationin Fig. 1, optimized with G09 software of (HL) performed at DFT theory level, using the functional RB3LYP and basis set [6-311++G(d, p)]; the structural configuration of HL demonstrated by zero imaginary frequency has shown local-minima at the potential energy surface. From these calculations, the molecule has shown 111 fundamental vibrational modes that belong to C1 symmetry. These 111 vibrational modes are correspondingly distributed into 38 stretching, 37 bending and 36 torsional vibrations in the computed spectrum having 39 atoms by using (3N−6) formula.[13]

Results and Discussion

Mulliken Population Analysis

Mulliken atomic charges: describes exchange of charges and equalization of electronegativity in chemical reactions, determined by DFT-B3LYP [6-311++G(d, p)] computational method of HL organised in Table 1. More electronegativity atoms i.e. N7 & S17 acquire more negative charge simultaneously, more positive charge accumulated or development of acidic nature at C6, C10, and C2.

HOMO-LUMO Analysis and other Chemical Descriptors

Several energy gaps of different HOMO-LUMO orbitals are calculated from optimized configuration

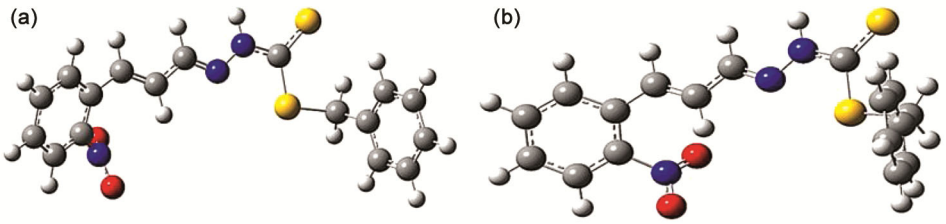

Fig. 1 — Optimized geometry of (HL) at RB3LYP-6-311G++(D,P) [(a) and (b) at diverse orientations]

Table 1 — Milliken atomic charges in coulombs (C) calculated by RDFT-B3LYP/ 6-311G ++ (d, p)

Atom	Charge	Atom	Charge	Atom	Charge
C1	−0.059	C11	−0.334	C21	−0.305
C2	−0.216	C12	−0.366	C22	−0.263
C3	−0.298	N13	−0.197	C23	−0.363
C4	−0.473	N14	0.463	C24	−0.327
C5	−2.420	C15	−0.484	O8	0.037
C6	2.451	S16	−0.631	O9	0.068
N7	−0.182	S17	0.299	C10	0.515
C18	−0.321	C19	0.905	C20	−0.161

of HL. These different energy gaps of HOMO-LUMO signify how strong the charge transfer mechanism could be and hence defines the hardness and softness of HL electronically. Global chemical reactivity can be predicted by Chemical potential and hardness. On the other-hand electrophilicity of a compound stands for its stabilization energy while getting extra electronic charges to the surrounding environment.[14,15] It also indicates how strong a molecule resides in exchange for an electronic charge with its surroundings. All these findings are stated in detail only after inter-frontier orbital analysis.

Canonical molecular orbitals of DFT calculations are important descriptors in figuring out the chemical reactivity of a molecule. Current investigation suggests, that in the HOMO canonical orbitals are all-over dispersed in the vicinity of molecular structure, meanwhile, in the lowest unoccupied molecular orbital LUMO, these are relatively localized. Other inner frontier orbitals like HOMO−1 and LUMO+1 also exhibit lower canonical orbital dispersion over the molecular geometry depicted in Fig. 2. In contrast, the canonical orbital distribution is somewhat more in phenyl moiety on HOMO−1. Hence, the ground state electronic transition from HOMO to excited state LUMO is the predominant flow of electrons from the cinnamic ring to the phenyl group. HOMO and LUMO energy differences are important parameters in determining the excitability of a (HL) Schiff base ligand; a decline in the topological resonance energy designates a smaller energy gap.[16] Computationally colour code depicts the charge distribution in chemical systems like red and green colour indicates positive and negative phases responsible for nucleophilic and electrophilic attack. Apart from HOMO-LUMO, electron affinity (EA) and vertical ionization potential (IE) are calculated for the optimized configuration. The calculated (IE) and (EA) are 7.624eV and −1.606eV, respectively. Other derivatives from these findings are chemical hardness of HL (η) 5.418eV, chemical potential (χ) 3.009eV, softness (S) 0.092eV and electrophilicity (ω) 0.835eV.

The HOMO–LUMO gap (ΔE) of the HL is 3.30eV. In general, lower chemical reactivity in compounds accounts for a higher energy gap while lower energy gap compounds display higher chemical reactivity and related energy to these inner frontier orbitals is well depicted in Table 2. As energy gap of the HL molecule is polarised since the energy gap is small, and hence adopts small kinetic stability, and high chemical reactivity is also known as soft molecules electronically.

Methodology for Assessing Antibacterial Activity

The antibacterial activity of HL was assessed using the Disk Diffusion Method (DDM), employing control

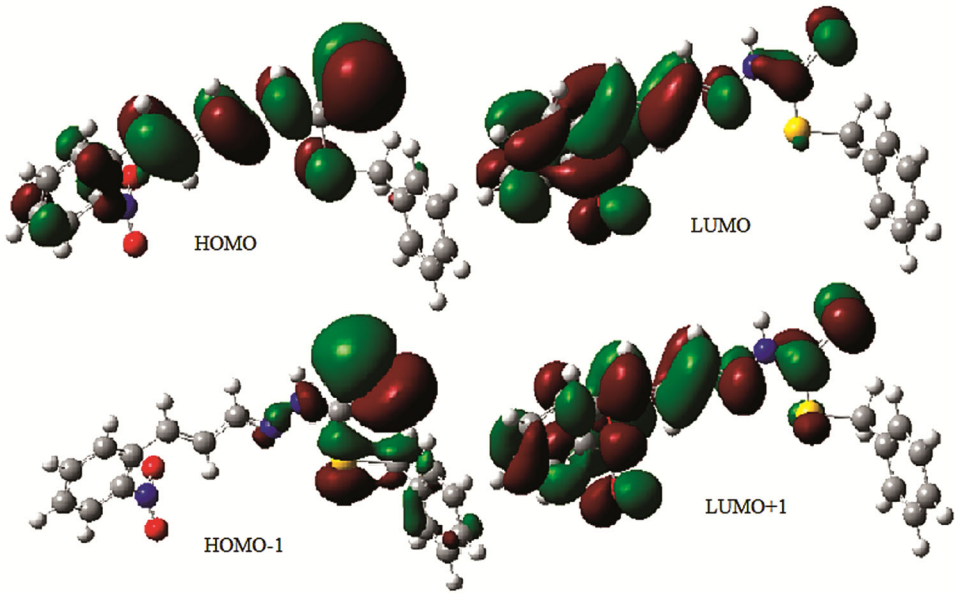

Fig. 2 — 3D Pictorial representation of frontier molecular orbitals of HL

Table 2 — Simulated FMO energies values of HL in eV

Parameters	HOMO	LUMO	Energy Gap	HOMO−1	LUMO+1
HL	−6.29eV	−2.99eV	3.30eV	−6.37eV	−2.44eV

concentrations of 10, 20, and 30 µg/mL on Mueller-Hinton agar plates. Triplicate disk diffusion assays were performed in accordance with Clinical and Laboratory Standards Institute guidelines.[17] Bacterial suspensions were prepared to match the 0.5 McFarland standard and uniformly inoculated onto sterilized agar plates using a sterile swab. Sterilized filter paper discs (6 mm diameter) were impregnated with known concentrations of the HL ligand, dried, and subsequently placed on the agar surface. Ciprofloxacin served as a positive control, while acetone was utilized as a negative control for result validation. The plates were incubated at 4°C for 24 hours to facilitate diffusion, after which they were incubated at 37°C for 12 hours to promote bacterial growth. The presence of a clear zone of inhibition around the discs indicated the antibacterial activity of HL, demonstrating its capacity to impede microbial growth.

Experimental and Theoretical FT-IR Analysis

The experimental and computed-one FT–IR of the HL under investigation is outlined in Fig. 3. Both experimental and theoretically calculated vibrational frequency modes along with their adjacent intensities and specific bind assignments are projected in Table 3. Aromatic ring coupled vibrations are depicted at 1625 and 1400 cm^{-1}. The calculated frequencies (1593 and 1502 cm^{-1}) of C-C bond stretching vibrations. Subsequently, the simulated frequencies are 1623 and 1526 cm^{-1}. The experimental peaks from 758–522cm^{-1} are allocated to C-C-C out-of-plane and in-plane twisting vibrations of the HL, the computed in-plane C-C-C bending vibrations and out-of-plane vibrations exhibit excellent agreement with the experimental values, indicating a strong correspondence between the experimental and simulated results. This alignment suggests that both sets of vibrations are in close agreement, reinforcing the consistency of the data.

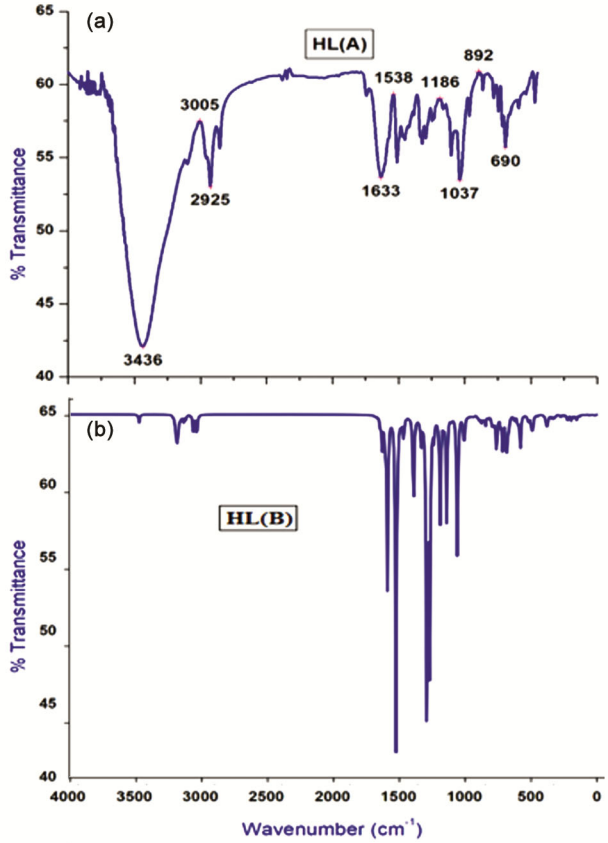

Fig. 3 — Calculated and simulated (A&B) IR spectra of HL

Stretching vibrations of νC = S & νC-S were detected in discrete ranges with other stretching vibrational modes from 689–964 cm^{-1}, while from simulated results, the stretching bands are observed at 678–1057 cm^{-1} evidently specifies the existence of thioketo form of the HL.

The stretching vibration for C-H of aromatic rings is normally anticipated to appear in 3100–3000 cm^{-1} region. The prominent band of HL at 3005 cm^{-1} corresponds to C-H stretching vibrations, same value is in close conformity with the simulated value at 3034 cm^{-1}, although the stretching vibrations of alkyl groups arise at very lower frequencies than aromatic rings.

Broad range vibrations available at 1360–1080 cm^{-1} is depiction of C-N stretching, difficult to find because of jagged intensities in FT-IR spectrum. Available vibration at 1634 cm^{-1} is allotted to C-N absorption peak in the hydrazides while the corresponding simulated vibration of HL lie at 1628 cm^{-1}. Usually, from literatures evidences for Schiff bases of dithiocarbazate stretching vibration of N-H displays at 3500–3250 cm^{-1}. Similarly, same band of HL is observed at 3438 cm^{-1} due to the N-H stretching frequency and its computational counter-part is observed at 3472 cm^{-1}.

Physicochemical and Spectral Characterizations

Experimental Yield: 3.01 g, 79.57%. m.p.: 189°C. IR (KBr), cm^{-1}: ν(NH) 3438, ν(C=N) 1510, ν(C=S) 1187, ν(N–N) 1102, ν(CSS) 1037, ν(CH) 3005, ν(C=C) 1634, ν(C-N_{nitro}) 1320, δ(CH) 1450. UV–Vis (Acetone), λ_{max}, nm (log ε, L $mol^{-1}cm^{-1}$): 396 (3.17), 386 (3.14), 400 (3.23), ^{1}H NMR (400 MHz, $(CD_3)_2CO$): δ 9.90 (s, 1H of NH), 8.01 (s, 2H-Aromatic proton), 7.87-7.83 (m, 3H-Aromatic proton), 7.71–7.49 (q, 3H-Aromatic proton),

Table 3 — Comparative study of the experimental (FT-IR) and simulated (FT-IR) of (HL) performed at DFT-RB3LYP level

Experimental Wave No. [cm^{-1}]	Calculated (scaled) Wave No. [cm^{-1}]	Vibrational band assignments PED (%)
3438	3472	ν_{str}(N14-H32)100
	3210	ν_{str}(C2-H26)18+ν_{str}(C4-H28)79
	3197	ν_{str}(C2-H26)74+ν_{str}(C4-H28)17
	3190	ν_{str}(C20-H35)92
	3185	ν_{str}(C1-H25)95
	3182	ν_{str}(C11-H30)99
	3181	ν_{str}(C20-H35)95
	3173	ν_{str}(C20-H35)95
	3172	ν_{str}(C1-H26)93
	3163	ν_{str}(C20-H35)87
	3155	ν_{str}(C21-H36)87
	3136	ν_{str}(C10-H29)99
3005	3118	ν_{str}(C18-H33)99
2925	3061	ν_{str}(C18-H33)99
2853	3034	ν_{str}(C12-H31)100
	1675	ν_{str}(C10-C11)56+δ(H29-C10-C11)11
	1644	ν_{str}(C1-C2)58
	1643	ν_{str}(C20-C21)60+δ(H35-C20-C21)18
1634	1628	ν_{str}(N13-C12)65
	1623	ν_{str}(C19-C24)65
	1606	ν_{str}(O8-N7)10+ν_{str}(C3-C4)38+δ(C1-C2-C3)10+δ(C2-C3-C4)10
	1587	ν_{str}(O8-N7)80
	1526	ν_{str}(C19-C24)10+δ(C20-C21-C22)12+δ(H35-C20-C21)57
	1523	ν_{str}(N14-C15)12+δ(H32-N14-N13)60
1510	1511	ν_{str}(C3-C4)14+ν_{str}(C4-C5)10+δ(H25-C1-C2)46
	1485	ν_{str}(C19-C24)24+δ(H37-C22-C23)50
	1469	δ(H26-C2-C3)51
1450	1464	δ(H34-C18-H33)52+τ(H33-C18-S17-C15)40
	1390	ν_{str}(O8-N7)75+δ(O8-N7-O9)12
	1383	ν_{str}(N13-C12)11+δ(H31-C12-N13)49
	1362	δ(H35-C20-C21)82
	1348	ν_{str}(C1-C2)25+δ(H29-C10-C11)34
	1339	ν_{str}(C19-C24)71+δ(H33-C18-S17)17
	1332	ν_{str}(C1-C2)30+δ(H25-C1-C2)11+δ(H29-C10-C11)16
1320	1314	δ(H30-C11-C12)59
	1288	ν_{str}(N14-C15)41+δ(H25-C1-C2)18
	1278	τ(H33-C18-S17-C15)45+δ(H34-C18-H33)36
	1266	ν_{str}(N14-C15)15+ν_{str}(C4-C5)11+δ(H25-C1-C2)31+δ(H29-C10-C11)12
	1235	
	1224	ν_{str}(C4-C5)40+δ(H25-C1-C2)10+δ(C4-C5-C6)11
	1205	ν_{str}(C18-C19)39+δ(H35-C20-C21)16+δ(C19-C24-C23)11
	1189	ν_{str}(C20-C21)21+δ(H35-C20-C21)74
	1188	δ(H26-C2-C3)66+ν_{str} (C1-C2)15 δ(H33-C18-S17)41
1187	1186	ν_{str}(C11-C12)26+δ(H33-C18-S17)20
	1181	ν_{str}(C19-C24)16+δ(H33-C18-S17)62
	1160	ν_{str}(C3-C4)19+ν_{str}(N7-C5)10+δ(H26-C2-C3)26
	1138	ν_{str}(N13-N14)65
	1110	ν_{str}(N7-C5)13+δ(C1-C2-C3)19+1104 δ(H25-C1-C2)10+δ(C2-C3-C4)14
1102	1101	ν_{str}(C19-C24)40+δ(H37-C22-C23)30
	1063	ν_{str}(C1-C2)65+δ(H25-C1-C2)16
	1057	ν_{str}(S16-C15)51

(*Contd.*)

Table 3 — Comparative study of the experimental (FT-IR) and simulated (FT-IR) of (HL) performed at DFT-RB3LYP level (*Contd*.)

Experimental Wave No. [cm^{-1}]	Calculated (scaled) Wave No. [cm^{-1}]	Vibrational band assignments PED (%)
1037	1050	δ(H35-C20-C21)20+ν_{str}(C20-C21)35+δ(C20-C21-C22)33
	1017	ν_{str}(C20-C21)42+δ(C20-C21-C22)45
	1007	τ(H26-C2-C3-C4)77
	1002	τ(H35-C20-C21-C22)72+τ(C20-C21-C22-C23)20
	1001	τ(C1-C2-C3-C4)18+τ(H26-C2-C3-C4)70
	987	τ(H35-C20-C21-C22)77+τ(C20-C21-C22-C23)11
964	952	τ(H30-C11-C12-N13)78
	934	τ(H35-C20-C21-C22)84
	900	τ(H25-C1-C2-C3)57+σ(N7-C4-C6-C5)12
894	889	δ(C1-C2-C3)16+δ(O8-N7-O9)16
	875	δ(H33-C18-S17)13+τ(H34-C18-S17-C15)43
	863	τ(H29-C10-C11-C12)67
	856	τ(H35-C20-C21-C22)92+τ(H37-C22-C23-C24)32
	843	ν_{str}(C3-C4)22+δ(O8-N7-O9)38
	820	ν_{str}(C18-C19)25+δ(C21-C22-C23)41
	796	τ(H25-C1-C2-C3)39+σ(N7-C4-C6-C5)37
	781	τ(C19-C24-C23-C22)11
	758	σ(N7-C4-C6-C5)19+τ(H25-C1-C2-C3)30+τ(H25-C1-C2-C3)16
	729	τC3-C4-C5-C6)52
715	712	τ(H37-C22-C23-C24)53+τ(C19-C24-C23-C22)35
689	686	ν_{str}(S16-C15)10+ν_{str}(S17-C18)18
	678	ν_{str}(S17-C18)27+δ(C1-C2-C3)15
	664	ν_{str} (S17-C18)14+δ(C3-C4-C5)12
	635	δ(C20-C21-C22)75+δ(C19-C24-C23)11
	624	ν_{str}(S17-C15)14+δ(C3-C4-C5)40
	598	ν_{str}(S16-C15)10+δ(O9-N7-C5)12+δ(C11-C12-N13)17+δ(N13-N14-C15)11
	579	δ(O9-N7-C5)13+τ(C1-C2-C3-C4)19+τ(H32-N14-N13-C12)77
563	571	δ(C21-C22-C23)22+δ(C19-C24-C23)14
	522	σ(S16-N14-S17-C15)76
	513	δ(O9-N7-C5)10+τ(C2-C3-C4-C5)17
	493	ν_{str}(S17-C15)28
	484	ν_{str}(S17-C18)10+τ(C20-C21-C22-C23)26
	448	δ(C5-C6-C10)29+ν_{str}(S17-C15)14
	414	τ(H35-C20-C21-C22)19+τ(C20-C21-C22-C23)77
	395	δ(O9-N7-C5)14+τ(C1-C2-C3-C4)11+τ(C2-C3-C4-C5)23
	380	δ(C15-S17-C18)19
	371	τ(C11-C12-N13-N14)37
	351	δ(C15-S17-C18)34+τ(H34-C18-S17-C15)14
	335	δ(S16-C15-S17)51
	318	τ(C10-C11-C12-N13)14
	274	δ(S17-C18-C19)15+τ(C20-C21-C22-C23)13
257	294	δ(N7-C5-C4)17
	220	δ(N7-C5-C4)20
	150	δ(N14-C15-S17)10+δ(C10-C11-C12)14
	127	σ(C18-C20-C24-C19)46
	94	δ(C12-N13-N14)12+τ(O9-N7-C5-C4)15
	85	σ(C18-C20-C24-C19)51

ν-stretching: δ-bending: τ-torsional: σ-out of plane

7.43–7.00 (m, 2H), 4.00 (s, 2H, CH_2), (Fig. 4). ^{13}C-NMR (CDCl3): 40, 76–82, 113–133, and 141–145 ppm, (Fig. 5). +ESI-MS (m/z): [359.05= HL] calculated mass = 357.46 (Fig. 6).

Electronic Spectra Analysis

Time-Dependent Density Functional Theory (TDDFT) calculation is performed to analyze electronic spectra of HL in acetone. Comparative UV-

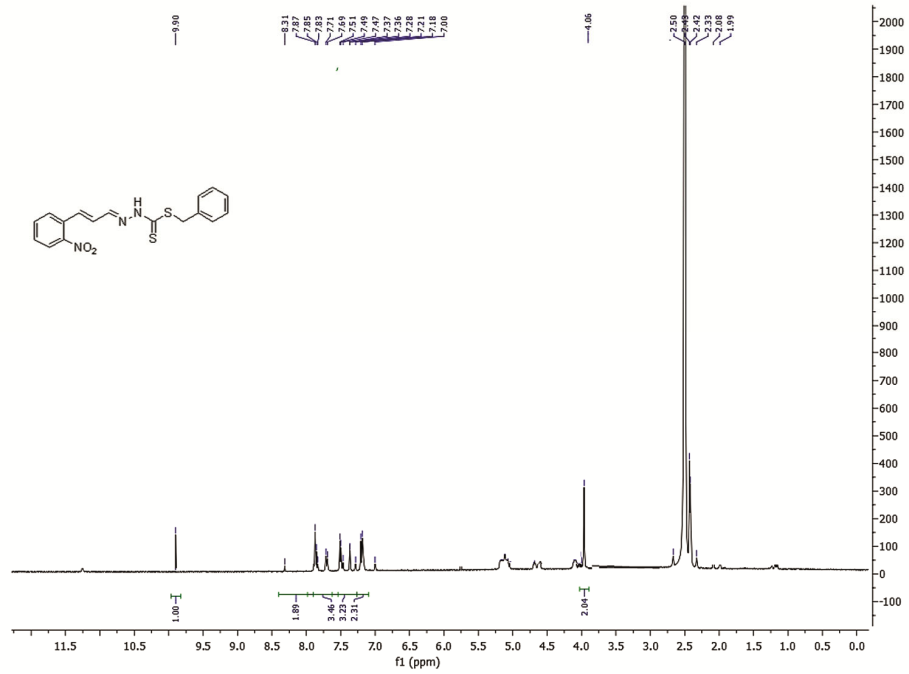

Fig. 4 — ^{1}H NMR spectra of HL

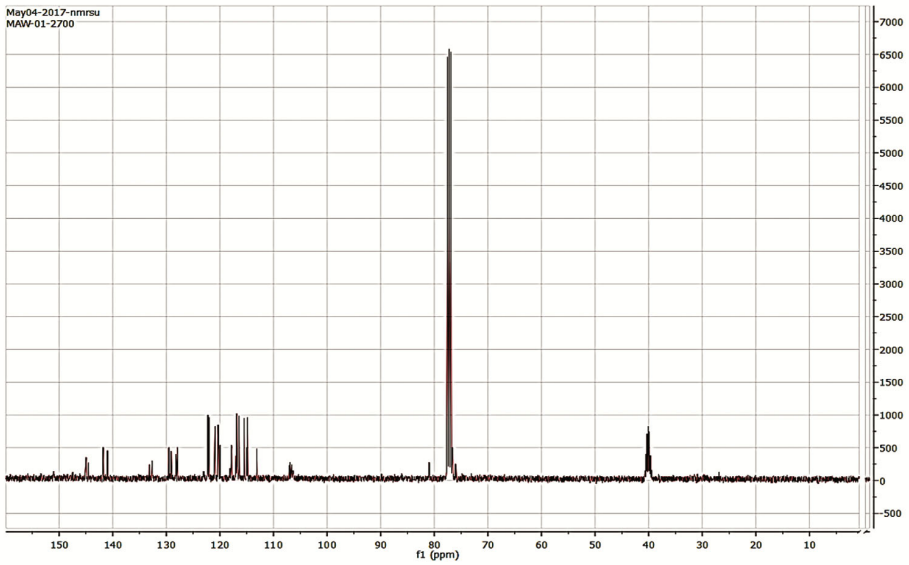

Fig. 5 — ^{13}C NMR spectra of HL

Vis spectra for experimental and computational output are depicted in Table 4 and Fig. 7. In Table 4, observed wavelengths at which experimental and computational electronic transitions take place are shown followed by descriptions of the concerned energy barrier, corresponding oscillator strength with associated molecular orbital, and assigned nature. The electronic transitions at 352 and 469 nm correspond to calculated 357 and 468 nm, respectively. The electronic transition at 357 nm is n→π* in nature, is due to the electronic transition from HOMO to LUMO+1. Localized non-bonded electronic charges get populated in the region of NO_2 attached to a benzene ring. On other hand, transition peaks at 468 nm consequence of the electronic jump from HOMO to LUMO. This transition is also n→π* in nature and exhibits similar redistribution of electronic cloud within the cavity of HL as observed for 469 nm.

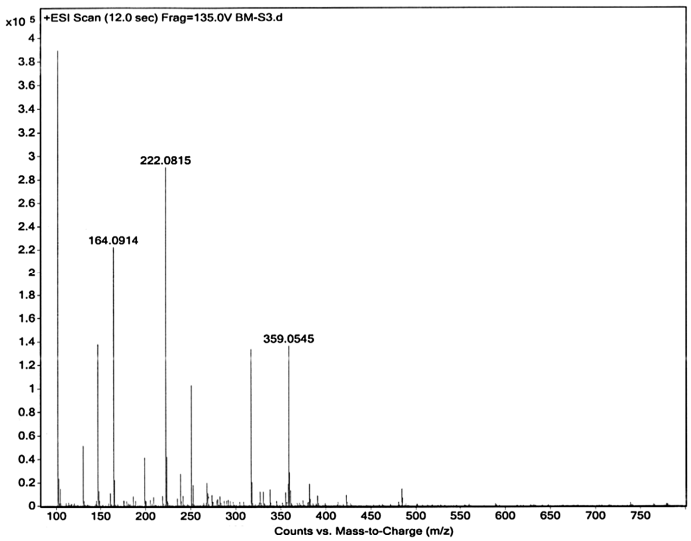

Fig. 6 — Mass spectra of HL

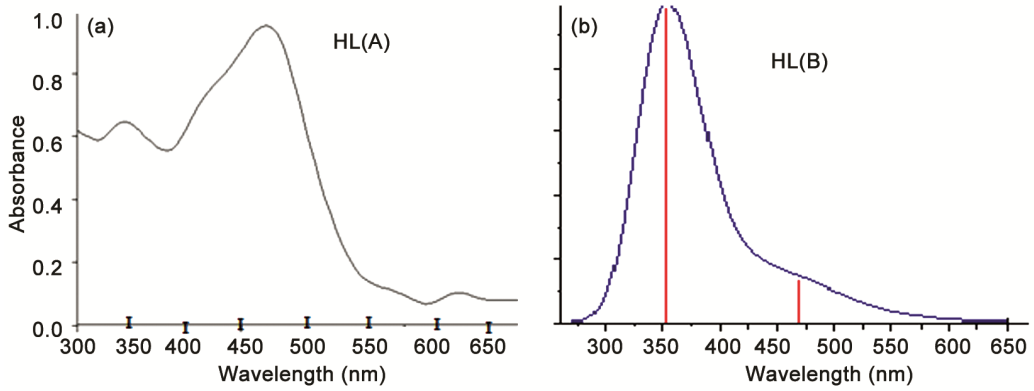

Fig. 7 — Experimental & Theoretical UV-Spectra of HL in acetone solvent

Table 4 — The experimental and computed wavelength (nm), absorbance and oscillator strengths(f) of HL in acetone solution

Experimental	Simulated results by B3LYP/6-311++g(d,p) basis set				
λ(nm)	λ(nm)	E(nm)	f (Oscillator Strength)	Major Contribution	Assignment
352	357	1431.86 nm	1.11	HOMO→LUMO+1(68%)	n→π*
469	468	1336.04 nm	0.17	HOMO→LUMO (91%)	n→π*

MESP Analysis

The Molecular Electrostatic Surface Potential (MESP) mapping is a technique used to calculate electrostatic potential onto the iso-electronic density surface. The MESP is certainly inferred as a colour spectrum, in consequence this, it is treasured in the research of molecular surface analysis with its connection between physiochemical and also H-bond relations. The HL electrostatic potential, computed at the 0.020e/Å^3 iso-density surface is depicted in Fig. 8. MESP colour code mapping ranges from −5.43 to +5.43 with dark-blue colour representing tremendously electron-deficient areas and red colour designates electron-rich regions, prone to nucleophilic and electrophilic attacks.

In Fig. 8, the nitro group of the cinnamic portion is largely depicting a negative region. Characteristically the maximum positive region is disseminated on the N13 and N14-H of dithiocarbazate group. The intermolecular interactions of different groups covering a particular area are provided by these above-mentioned locations. The MESP surfaces gives prior indications regarding feasible reactive positions i.e., electrophilic surface attack at O9-N7 = O8, and nucleophilic surface attack at N13 & N14-H, Moreover, it's also Evident from Fig 8, the HOMO of

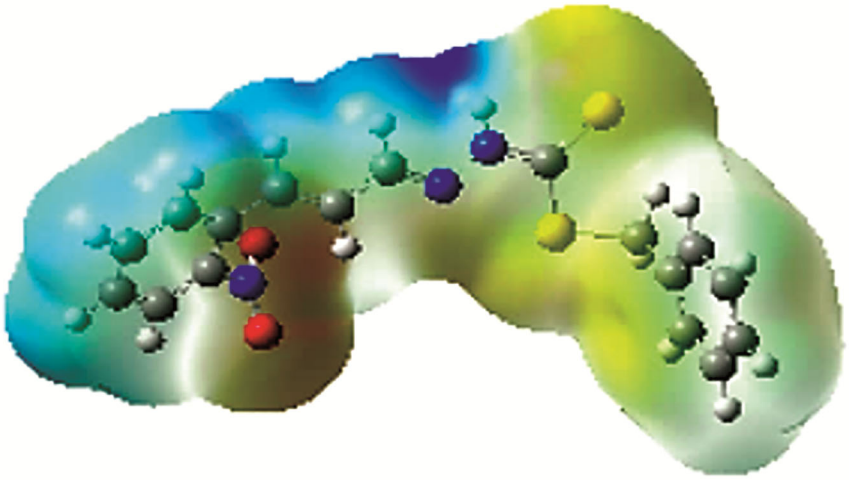

Fig. 8 — MESP attained by RB3LYP/6-311++G(d,p) level of HL ligand

Table 5 — Natural bond order (NBO) E^2 value

Donor	Acceptor	E(2) [kcal/mol]	E(j)-E(i) [a.u.]	F(i, j) [a.u.]	Donor	Acceptor	E(2) [kcal/mol]	E(j)-E(i) [a.u]	F(i, j) [a.u]
πC1-C6	π*C2-C3	20.834	0.283	0.069	LP(2) O9	σ*C5-N7	12.051	0.561	0.073
	π*C4-C5	20.633	0.274	0.069		σ*N7-O8	18.812	0.722	0.105
πC2-C3	π*C4-C5	23.334	0.274	0.071	LP(1) N14	π*C12-N13	29.382	0.282	0.084
πC10-C11	π*C12-N13	19.121	0.283	0.066		π*C15-S16	66.262	0.214	0.108
LP(2) O8	σ*C5-N7	11.862	0.561	0.073	LP(2) S17	π*C15-S16	43.183	0.166	0.079
LP(2) O8	σ*N7-O9	18.605	0.711	0.104	π*C1-C6	π*C10-C11	47.213	0.025	0.057
LP(3) O8	π*N7-O9	145.633	0.162	0.138	π*C12-C13	π*C10-C11	26.303	0.046	0.067

HL of the cinnamic group is more populated than the phenyl core.

NBO Analysis

To evaluate the donor (i) and acceptor (j) interaction and stabilization energy E(2) in the natural bond order (NBO) basis is calculated by second order perturbation approach.[18–20] By analysis, this system shows some contribution to the π and σ electron delocalization corresponds to the donor–acceptor interactions determined by following equation.

$$E^2 = \Delta E_{i,j} = q_i \frac{2F(i,j)}{\varepsilon_i - \varepsilon_j}$$

From Table 5, Stronger perturbation energies interactions are due to LP (3)O8→π*(N7-O9)(145.63 kJ/mol.), LP(1)N14→π*C15-S16(66.26kJ/mol), LP(2) S17→π*C15-S16(43.18 kJ/mol.) & π*C1-C6→π* C10-C11 (47.21kJ/mol). Also, lone pair at O8 get strongly dispersed over the nearby π* orbital of N7-O9, these strong conjugation plays a dominant role in the stabilization of HL molecule.

Raman Spectra Analysis

Instrument used in experimental Raman spectra determination for HL was (JYH LABRAM-HR visible (400–1100 nm) at lens ($50x^{LWD}$), power (25 mW), hole (1000), grafting (1800), Laser frequency (473 nm), slit (100) and DFT calculation by (G09 software) at RB3LYP method & basis set 6-311G++(d, p). Some prominent peaks for νC=N→(1600 cm^{-1})=(1626 cm^{-1}), νC=S→(1118 cm^{-1})=(1136 cm^{-1}),νC-H→(3132 cm^{-1})= (3062 cm^{-1}), ν(NH)→(3188 cm^{-1})=(3187 cm^{-1}) and δ(N-H)→(1558 cm^{-1})=(1519 cm^{-1}) are evidently shown in Fig. 9 (A(Experimental) and B(Theoretical).[21]

TG Analysis

To evaluate the thermal behavior of (HL) by TGA-50 SHIMADZU-00652 instrument at a heating rate of 10°C/min under a N_2 atmosphere by thermogravimetric analyses (TGA) are conducted. The onset of the first degradation in WBPEA-PMF-80 was found to be at 181°C. The disintegration of the ligand (HL) started at 181°C. Further, the thermograms of the ligand reveal a steep decomposition up to 516°C and concluded on results that HL is found to be thermally stable shown in Fig. 10.

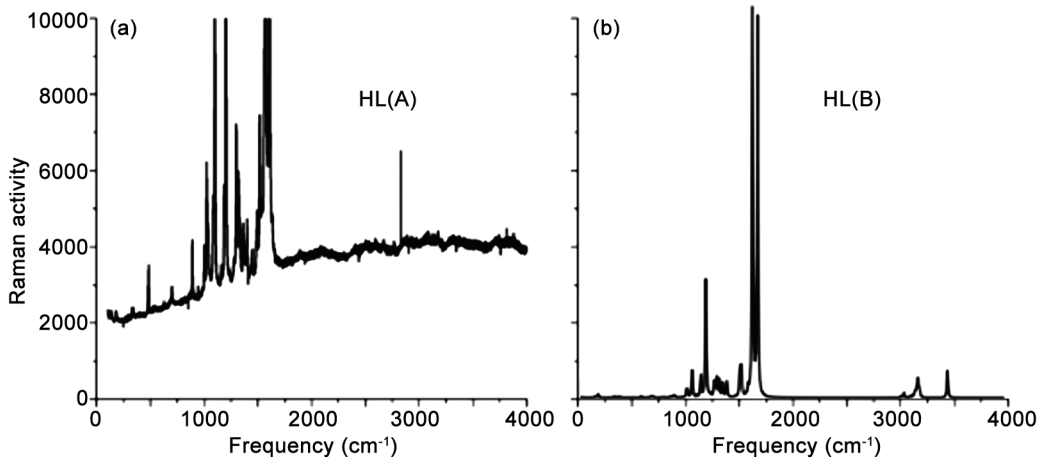

Fig. 9 — Raman spectra of HL (A&B)

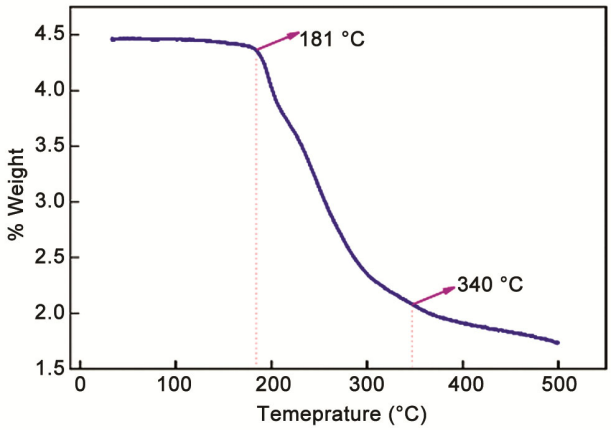

Fig. 10 — TGA Curve of HL

Antibacterial Results

Customarily infection-causing strains *E. coli* and *S. aureus* bacteria display prominent antibacterial sensitivity results towards HL. Ciprofloxacin drug (positive control) inhibition zone diameter was correlated with the antibacterial activity results of against *E. coli* ATCC 25922, *S. aureus* ATCC 6538-Pat various HL concentrations. Results (inhibition zone diameter results) acquired by mean deviation against *E. coli* and *S. aureus* of the standard drug were 23.3, 37.2, 51.1 and 21.01, 33.11, 49.07 mm and 26.03, 37.06, 49.06 and 19.2, 35.3, 46.07 mm of HL at 10, 20 and 30 µg/mL concentration shown in Figs 11 & 12. It was found that the activity proportionally surges with the rise of HL concentration also validated by previous findings.

Molecular Docking Studies

DNA Docking

3D structure of HL was designed by Marwin sketch Version 6.1.3 & Gastegier charges and Windows XP

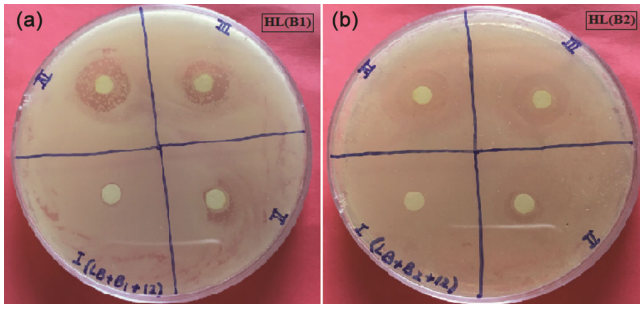

Fig. 11 — Inhibition zone diameterat different doses of HL against *E. coli* [B1] and *S. aureus* [B2]

operating system was employed to achieve docking results. After preparation of the HL molecule (drug) merging of non-polar hydrogens performed and same designed file has been saved in PDBQT format by employing AutoDock Tools (ADT) 4.2. DNA (PDB ID: 1BNA) X-ray crystal structure availed from (http://www.rcsb.org/pdb) website source for Protein Data Bank. Employing (ADT) 4.2. (AutoDock Tool) above saved file was refined & cleaned from the uneven water molecule and other moieties, then PDB format of DNA was saved in PDBQT file format. The ally between two popular docking programs i.e. AutoDock Vina & AutoDock (4.2) and PyMOL are represented by a plugin. For the setup of the docking program, the collective result of these two software programs made effective practice of Python script collection (AutoDock Tools) and for prominent hydrophobic interactions of HL with DNA Ligplot package employed to access the results.[22]

HL 3D interactions with DNA (Fig. 13) displayed that it has chosen DNA with binding energy −19.6648 kJ/mol. simultaneously, nitrogen-containing nucleobases Dg10, Dc9, Dc8, Dc15, & Dg14 binds with it, through a

web of hydrophobic interactions confirmed by 2D interactions of HL (Fig. 13). In the DNA-HL adducts a total number of hydrogen bonds was formed two, DG' 14H: N of C = N group with bond length (3.47Å) and DG' 14H: O of Nitro group (3.40Å) respectively. Binding affinity of the molecular systems containing halogen atoms show lesser affinity than nitro substituents on phenyl rings in molecular systems.

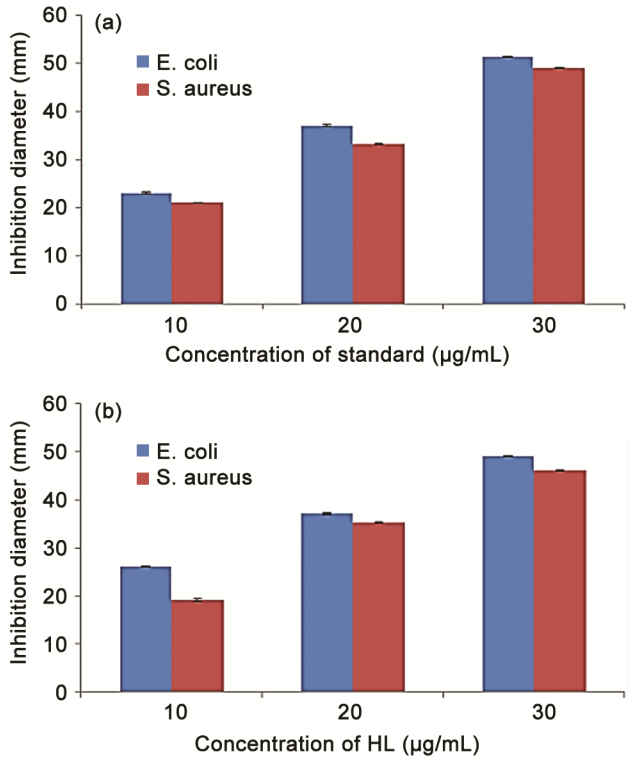

Fig. 12 — Positive Control inhibition diameter (a) and (b) of HL against *E. coli* & *S. aureus*

Protein Docking

The binding energy is quite good at −20.5016 kj/mol, the docking results of (3C5W) protein for HL compound in the study evidently express extensive binding affinities towards 3C5W. The hydrogen bonding pattern is shown in Fig. 14, along with hydrophobic interactions and cation-π interactions of HL with the binding site residues. Remarkably, the compound is displaying H-bond interactions with the well-maintained residues of the coenzyme binding motif such as TRY, GLY, and ASP, in Fig. 14, which also shows the binding posture of the HL-3C5W complex. H bonding interactions are the side chains of GLY, ASP, with the oxygen atoms of the nitro substituent of phenyl ring (3.34Å) & (3.30Å). Also, cationic π-interaction is shaped with the nitrogen atom (3.22Å) of the dithio group by the side chain amine of TRY.[23,24]

2019-nCoV Main Protease Docking

After the determination of DNA & protein molecular docking, we next studied its behavior towards 2019-nCoV main protease file (PDBID 7BRO). The preparation of the target, ligand, grid and docking parameter files of HL were done by employing all the above-mentioned docking software packages. The binding interactions (Fig. 15) with three different patterns HL1 = 2019-nCoV main protease file (PDBID 7BRO), HL2 = Zoomed grid interactions & HL3 = Normal grid interactions along with the binding free energies (Gb) and hydrogen bond interactions. The free energy of binding interaction is −4.8 kcal/mol. along with the key amino acid residues interacting with the 2019-nCoV main

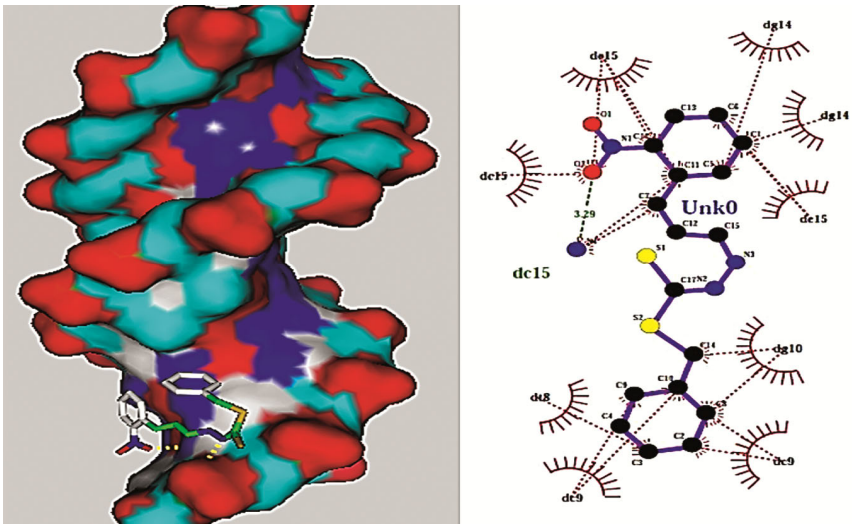

Fig. 13 — 3D and 2D DNA docking images and of HL

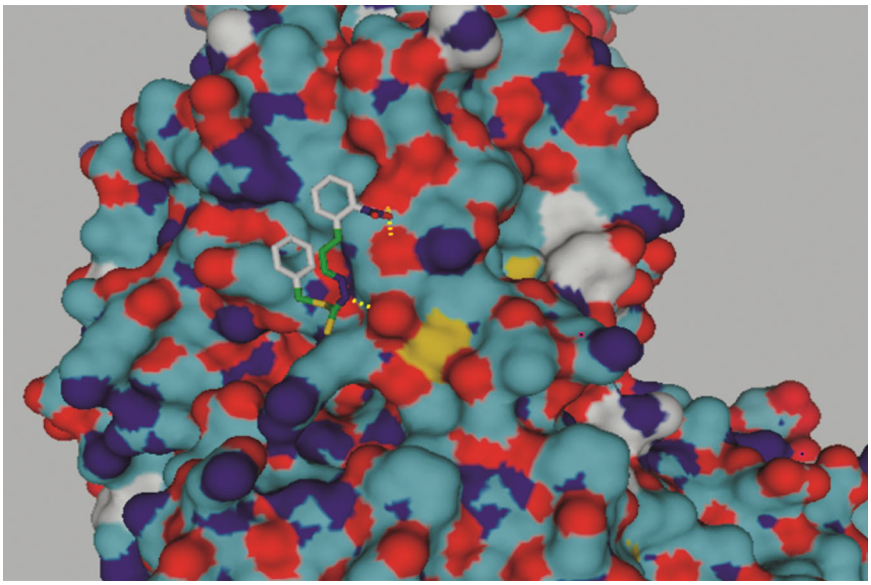

Fig. 14 — 3D Protein docking images of HL

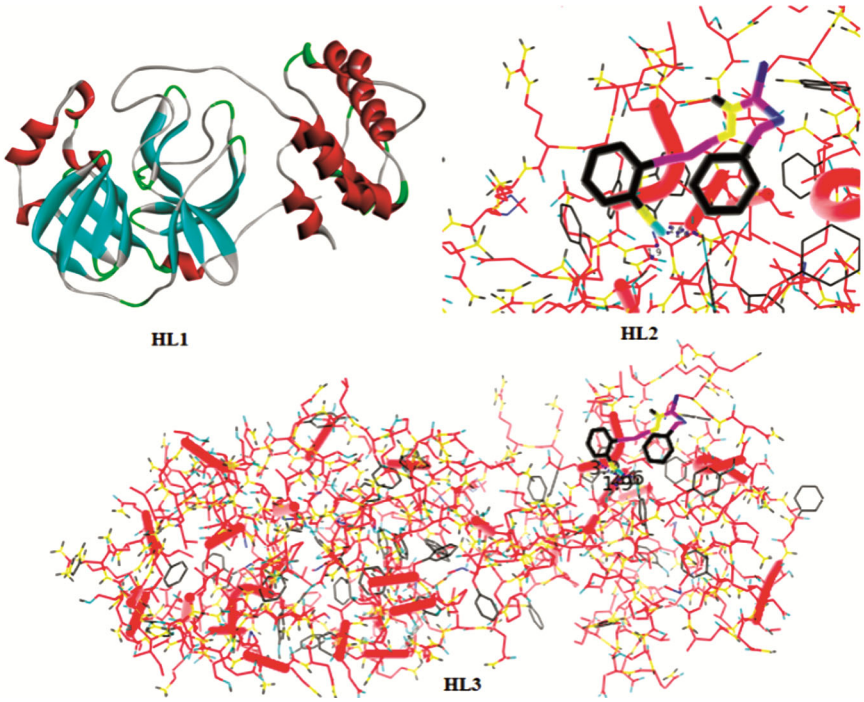

Fig. 15 — Best 3D grid of HL & 2019-nCoV main protease

protease. It is seen from results that 2019-nCoV main protease engages with HL through four favorable hydrogen-bond interactions and electrostatic interactions (charge-charge) interactions as THR199/ HG1, LEU287/O and TYR239/HH. Although nine binding interactions has been obtained however the highlighted interaction is the best one with lowest binding energy & four hydrogen bonding sites and thus these prominent results have theoretically confirmed that HL is the best 2019-nCoV main protease inhibitor.[25,26]

Conclusions

In the present study, novel dithiocarbazate-based Schiff base molecules have been synthesized and characterized utilizing a range of spectroscopic techniques and thermogravimetric analysis (TGA). To corroborate the experimental findings, computational

tools such as Gaussian 09 and VEDA-4 were employed for the better conformity of results. The inhibition diameters against both gram-positive and gram-negative bacterial strains were meticulously evaluated. The ligands exhibited robust binding interactions with proteins (3C5W) and the main protease (7BRO), resulting in comparatively high binding constants. This research elucidates a significant gap in the literature: the exploration of innovative bioactive alkyl/aryl nitrogen-sulfur (NS) chelating metal complexes as single crystals, aiming to achieve enhanced nano-bio interactions and a diverse array of potential electronic applications.

Acknowledgements

Rayees A. Bhat thanks CSIR-HRDG, Govt. of India [Grant No. 09/961(0020)/2020-EMR-I] for funding this research.

References

1 Curtius T & Heidenreich K, Die Hydrazide und Azide der Kohlensäure, *J Für Praktische Chemie*, **52** (1895) 454–489.

2 Husain A, Nami S A A & Siddiqi K S, Synthesis, characterization and biocidal activities of heterobimetallic complexes having tin (IV) as a padlock, *J Mol Str*, **970** (2010), 117–127.

3 Hazari S K S, Kopf J, Palit D, Rakshit S & Rehder D, Oxidovanadium (IV) complexes containing ligands derived from dithiocarbazates–Models for the interaction of VO2+ with thiofunctional ligands, *Inorg Chim Acta*, **362** (2009) 1343–1347.

4 Malakar K, Sohtun W P, Srinivasan V, Saravanan D & Velusamy M, Molecular design and synthesis of dithiocarbazate-based potential biomaterials: Crystal structure, apoptotic activity and protein binding studies, *J Mol Str*, **1285** (2023) 135388.

5 Nanjundan N, Narayanasamy R, Butcher R J, Jasinski J P, Velmurugan K, Nandhakumar R, Balakumaran M D, Kalaichelvan P T & Gnanasoundari V G, Synthesis, crystal structure, biomolecular interactions and anticancer properties of Ni (II), Cu (II) and Zn (II) complexes bearing S-allyldithiocarbazate, *Inorg Chim Act*, **455** (2017) 283–297.

6 Hu L, Wang H, Xu X, Zhang M, Tian X, Wu J, Zhou H, Yang J & Tian Y, A small-molecule with large two-photon action cross-section serves as the membrane-permeable probe for live cells imaging and bacteria viability, *Sens and Act B: Chem*, **241** (2017) 1082–1089.

7 Palaniappan M, Nagaraj K, Rangappan R, Wadaan M A, Ghodake G S, Vediyappan J, Arumugam S, Manogaran T, Nagaraj K & Karthikeyan A, Synthesis, characterization and biological evaluation of methyl dithiocarbonate-acenaphthenequinone MDTCZ-ACQ) schiff base ligand and its coordination complexes with copper, nickel, zinc, and cobalt, *J Ind Chem Soc*, **102** (2025) 101615, https://doi.org/10.1016/j.jics.2025.101615.

8 Bhat R A, Kumar D, Malla M A, Bhat S U, Khan M S, Manzoor O, Srivastava A, Naikoo R A, Mohsin M & Mir M A, Synthesis, characterization, computational studies and biological evaluation of S-benzyl-β-N-[3-(4-hydroxy-3-methoxy-phenylallylidene)]dithiocarbazate, *J Mol Str*, **1156** (2018), 280–289.

9 Bhat R A, Kumar D, Singh K, Srivastava A, Shahzad Khan M, Malla MA, Ganie J A & Mir M A, Synthesis and Spectral Characterization of Zn (II) Complex of S-benzyl-β-N-[3-(4-hydroxy-3-methoxy-phenylallylidene)]dithiocarbazate: An approach to antibacterial, thermal studies and DFT calculations, *J Mol Str*, **1199** (2020) 126877, https://doi.org/10.1016/j.molstruc.2017.11.051.

10 Hossain M E, Atam M E, Begum J, Ali M A & Nazimuddin M, Synthesis, characterization and biological activities of some nickel (II) complexes of tridentate NNS ligands formed by condensation of 2-acetyl-and 2-benzoylpyridines with S-alkyldithiocarbazates, *T Met Chem*, **18** (1993) 497.

11 Tahir M I M, Osman U M, Hassim M F N, Safayi N N S Z, Arshad S, Nizar S N A M, Fazira I A R & Sapari S, Structural and computational analysis of a nickel(II) complex with S-benzyldithiocarbazate Schiff base ligand: Synthesis, X-ray crystallography, MEP, HOMO-LUMO, Hirshfeld surface analysis, and molecular docking, *J Mol Str*, **1321** (2025) 139760.

12 Frisch M J, Trucks G W, Schlegel H B, Scuseria G E, Robb M A, Cheeseman J R,Montgomery J A, Vreven T, Kudin K N, Burant J C, Millam J M, Iyengar S S, Tomasi J, Barone V, Mennucci B, Cossi M, Scalmani G, Rega N, Petersson G A, Nakatsuji H, Hada M, Ehara M, Toyota K, Fukuda R, Asegawa J, Ishida M, Nakajima T, Honda Y, Kitao O, Nakai H, Klene M, Li X, Knox J E, Hratchian H P, Cross J B, Adamo C, Jaramillo J, Gomperts R, Stratmann R E, Yazyev O, Austin A J, Cammi R, Pomelli C, Ochterski J W, Ayala P Y, Morokuma K, Voth G A, Salvador P, Dannenberg J J, Zakrzewski V G, Dapprich S, Daniels A, Strain M C, Farkas O, Malick D K, Rabuck A D, Raghavachari K, Foresman J B, Ortiz J V, Cui Q,Baboul A G, Clifford S, Cioslowski J, Stefanov B B, Liu G, Liashenko A, Piskorz P, Komaromi I, Martin R L, Fox D J, Keith T, Al-Laham M A, Peng C Y, Nanayakkara A, Challacombe M, Gill P M W, Johnson B, Chen W, Wong M W, Gonzalez C & Pople J A, *Gaussian 03, Revision E.01* (Gaussian Inc, Pittsburgh, PA*)* 2003.

13 Bhat R A, Kumar D, Alam A, Mir B A, Srivastava A, Malla M A & Mir M A, Synthesis, characterization, thermal and DFT studies of S-methyl-β-N-(3-(2-nitrophenyl) allylidene) dithiocarbazate as anti-bacterial agent, *J Mol Str*, **1173** (2018) 72–80, https://doi.org/10.1016/j.molstruc.2018.06.061.

14 Tahir M I M, Osman U M, Hassim M F N, Safayi N N S Z, Arshad S, Nizar S N A M, Razak F I A & Sapari S, Structural and computational analysis of a nickel(II) complex with S-benzyldithiocarbazate Schiff base ligand: Synthesis, X-ray crystallography, MEP, HOMO-LUMO, Hirshfeld surface analysis, and molecular docking, *J Mol Str*, 1321(2025) 139760, https://doi.org/10.1016/j.molstruc.2024.139760.

15 Mushtaque M, Jahan M, Ali M, Khan M S, Khan M S, Sahay P & Kesarwani A, Synthesis, characterization, molecular docking, DNA binding, cytotoxicity and DFT studies of 1-(4-methoxyphenyl)-3-(pyridine-3-ylmethyl) thiourea, *J Mol Str*, **1122** (2016) 164–174.

16 Bhat R A, Singh K, Kumar D, Kumar A & Mishra P, Antimicrobial studies of the Zn (II) complex of S-benzyl-

β-(N-2-methyl-3-phenylallylidene)dithiocarbazate, *J Coord Chem*, **75** (2022) 1050–1062, https://doi.org/10.1080/ 00958972. 2022.2083962.

17 Wayne P A, Clinical and Laboratory Standards Institute: Performance standards for antimicrobial susceptibility testing: 20th informational supplement, *CLSI document M100-S20*. (2010).

18 Kavitha T, Pasupathi G, Marchewka M K, Anbalagan G & Kanagathara N, Structural and spectroscopic investigation of glycinium oxalurate, *J Mol Str*, **1143** (2017) 378–387.

19 Foster A J & Weinhold F, Natural hybrid orbitals, *J Am Chem Soc*, **102** (1980) 7211–7218.

20 Snehalatha M, Ravikumar C, Joe I H, Sekar N & Jayakumar V S, Spectroscopic analysis and DFT calculations of a food additive Carmoisine, *Spect Acta Part A: Mol and Biomol Spec*, **72** (2009) 654–662.

21 Ali I, Lone M N, Alothman Z A & Alwarthan A, Insights into the pharmacology of new heterocycles embedded with oxopyrrolidine rings: DNA binding, molecular docking, and anticancer studies, *J Mol Liq*, **234** (2017) 391–402.

22 Malakar K, Sohtun W P, Srinivasan V & Velusamy M, Synthesis, crystal structure and protein binding studies of a binuclear copper (I) complex with triphenylphosphine based dithiocarbazate, *Inorg Chem Comm*, **157** (2023) 111195.

23 Parekh J, Inamdhar P, Nair R, Baluja S & Chanda S, Synthesis and antibacterial activity of some Schiff bases derived from 4-aminobenzoic acid, *J Serb Chem Soc*, **70** (2005) 1155–1161.

24 Mumit M A, Pal T K, Alam M A, Md Islam A A, Paul S & Sheikh M C, DFT studies on vibrational and electronic spectra, HOMO–LUMO, MEP, HOMA, NBO and molecular docking analysis of benzyl-3-N-(2,4,5-trimethoxypheny-lmethylene)hydrazinecarbodithioate, *J Mol Str*, **1220** (2020) 128715.

25 Isalm A B M N, Habib M A, Hasan M M, Md. Hasan R, Karim K M R, Mahiuddin M, Yoshida T, Karim M R, Rahman S, Albrithen H, Alodhayb A N & Georghiou P E. Exploration of the synthesis, crystal structure, Hirshfeld surface analysis, binding properties, antibacterial activities, and molecular docking of a Schiff base nickel (II) Complex, *J Mol Str*, 1322 (2025) 140294, https://doi.org/10.1016/ j.molstruc.2024.140294.

26 Malakar K, Sohtun W P, Srinivasan V, Saravanan D & Velusamy M, Molecular design and synthesis of dithiocarbazate-based potential biomaterials: Crystal structure, apoptotic activity and protein binding studies, *J Mol Str*, 1285 (2023) 135388, https://doi.org/10.1016/ j.molstruc.2023.135388.